PHYSICS AND CHEMISTRY OF SOLID STATE
V. 26, No. 3 (2025) pp. 643-657
Section: Physics

DOI: 10.15330/pcss.26.3.643-657

Vasyl Stefanyk Carpathian National University

ФІЗИКА І ХІМІЯ ТВЕРДОГО ТІЛА
Т. 26, № 3 (2025) С. 643-657
Фізико-математичні науки

PACS: 87.85.jj; 81.20.Ka

ISSN 1729-4428 (Print)
ISSN 2309-8589 (Online)

Luciano Nascimento, Ana Cristina Figueiredo de Melo Costa

Amorphous Alloys Synthesized by High-Energy Milling: A Study on their Applications as Biomaterials

Laboratory of Ceramic Materials Synthesis, Federal University of Campina Grande, 882 Aprígio Veloso Street—Bodocongó, Campina Grande 58429-900, PB, Brazil, luciano.uepb@gmail.com

In this work, the amorphous alloys $Co_{69}Nb_{23}B_8$, $Fe_{78}Si_9B_{13}$, $Co_{68}Cu_{23}B_9$, and $Fe_{64}Nb_{28}B_8$ were synthesized by high-energy mechanical milling (HEM) and investigated as promising biomaterials for bone tissue regeneration. The synthesis was carried out with a 20 g powder load, a ball-to-powder weight ratio of 20:1, a rotation speed of 300 rpm, and a total milling time of 15 h, using ethyl alcohol (C_2H_6O) as a process control agent and an inert argon atmosphere. The amorphous alloys were characterized by X-ray diffraction (XRD), Fourier-transform infrared spectroscopy (FTIR), textural analysis, SEM, thermogravimetric analysis (TGA-DTA), magnetic measurements (VSM), mechanical testing, and in vitro cytotoxicity assays. Swelling degree analyses showed favorable results, indicating the potential biomedical applicability of the amorphous Co- and Fe-based alloys. Cytotoxicity tests revealed that the safe concentration, at which cell viability exceeded 70%, demonstrates promising potential for the use of these materials as metallic biomaterials for bone tissue regeneration and temporary orthopedic implants.

Keywords: Amorphous Alloys; Biomedical Applications; Bone Tissue Regeneration; High Energy Milling (HEM).

Received 22 October 2024; Accepted 17 September 2025.

Introduction

Increased life expectancy has led to a rapidly aging population, resulting in a higher incidence of bone diseases such as osteoporosis and fractures [1,2]. However, the search for ideal biomaterials remains one of the greatest challenges in medicine, for example for their use in bone tissue regeneration and implants [3]. There are many clinical reasons for developing new materials to replace human bone, for example in the reconstruction of defects, including the need for orthopedic implants that are corrosion-resistant and better adapted mechanically to their biological environment [4,5].

Bone is a mature connective tissue that ensures the function of our body, protects vital organs and forms a stable foundation for muscle and joint function. Bone also plays an important physiological role in supporting hematopoiesis and mineral homeostasis in our body and serves as the main protective barrier for vital organs [6]. Current surgical procedures for bone repair involve transplanting tissue grafts of natural origin or biomaterials developed using various methods such as powder metallurgy and rapid solidification [7].

The most commonly used reconstructive graft is an autologous graft, in which the patient's tissue is harvested from a donor site and transplanted into a damaged or defective recipient site [8]. These techniques have some limitations due to the limited availability of autologous grafts and the potential for trauma and invasive (surgical) procedures for the patient [9]. These limitations of grafts have led to the development and use of biomaterials as alternatives to bone tissue regeneration processes [10].

The purpose of biomaterials is to play a fundamental role in the regeneration of bone tissue by temporarily acting as a support structure that gradually distributes the load across the affected area, thereby providing a pathway for cell growth until the bone tissue is fully restored [11]. To achieve this, the structure must maintain its shape and appropriate mechanical properties throughout the regeneration process until the injured area is fully restored [12,13].

Amorphous alloys, as a metallic biomaterial, were first synthesized by Pol Duwez in 1960 in a binary metal alloy system $Au_{80}Si_{20}$ using a rapid cooling technique (in the range of 10^5 - 10^6 K s^{-1}) and have attracted the attention of researchers around the world due to their special properties [14, 15]. Amorphous alloys have a long-range disordered atomic structure and exhibit unique magnetic properties, high mechanical strength, low elastic modulus, good corrosion resistance, and satisfactory biocompatibility for biomedical applications [16].

Due to the importance of amorphous alloys, several technologies have been developed to obtain them over time, among which are the chilling of molten metal into ribbon forms (melt-spinning) [17], arc furnace casting (cooled metal mold) [18], centrifugal casting [19], gas atomization (hot or cold extrusion) [20], spray forming [21], chemical reduction [22], electrodeposition [23] and high energy milling (HEM) [24]. Among the methods mentioned, HEM stands out for being a powder processing technique that allows the production of homogeneous materials from the mixture of elementary powders [25]. Thus, the objective of the present work was the synthesis of amorphous alloys with the compositions $Co_{69}Nb_{23}B_8$, $Fe_{78}Si_9B_{13}$, $Co_{68}Cu_{23}B_9$ and $Fe_{64}Nb_{28}B_8$ by high energy milling (HEM) for applications of synthetic biomaterials in bone tissue regeneration. However, the use of the amorphous alloys $Co_{69}Nb_{23}B_8$, $Fe_{78}Si_9B_{13}$, $Co_{68}Cu_{23}B_9$ and $Fe_{64}Nb_{28}B_8$, synthesized by high energy milling (HEM), is being used for biomedical field. Then, their physical-chemical, magnetic, thermal, mechanical and biological properties were evaluated, in addition to their viability for application in the biomedical field.

I. Materials and methods

Elemental metal powders (99.9% purity, from Êxodo Científica − LTDA/Brazil) of Co, Fe, Nb, Cu, Si and B with nominal compositions of amorphous alloys $Co_{69}Nb_{23}B_8$, $Fe_{78}Si_9B_{13}$, $Co_{68}Cu_{23}B_9$ and $Fe_{64}Nb_{28}B_8$ (in *at. %*) were mechanically ground in a planetary ball mill (Fritsch Pulverisette 5). The powder mixture load was maintained at 20 g for all tests, as well as the ball-to-powder ratio by weight of 20:1. The test speed adopted was 300 rpm and a grinding time of 15 h. Finally, ethyl alcohol (C_2H_6O) (2 mL) was used as a process control agent (PCA) in the grinding medium to regulate the morphology of the homogenized powder and an argon atmosphere. The microstructural evaluation of the samples obtained from the mechanical alloy was performed by X-ray diffraction (XRD; BRUKER diffractometer, model D2 Phaser) using CuK_α radiation (λ = 1.54056 Å) produced at 45 kV and 40 mA. The diffraction angle (2θ) varied between 10º and 80º with a step of 0.012º and a time of 5 s. A TESCAN scanning electron microscope, model VEGA 3, operating in the voltage range of 5 or 10 kV, was used for the microstructural characterization. The samples were placed on a metal support (stage) and previously coated with a thin layer of gold (Au). Then, images were obtained at different points of the samples and at magnification in the order of 100 kx. From the analysis of the images, it was possible to observe the surface morphological modifications in the amorphous alloys $Co_{69}Nb_{23}B_8$, $Fe_{78}Si_9B_{13}$, $Co_{68}Cu_{23}B_9$ and $Fe_{64}Nb_{28}B_8$. The thermal studies of the amorphous powders of $Co_{69}Nb_{23}B_8$, $Fe_{78}Si_9B_{13}$, $Co_{68}Cu_{23}B_9$ and $Fe_{64}Nb_{28}B_8$ were collected after grinding, using differential thermal analysis (DTA) and thermogravimetric analysis (TGA) equipment from SHIMADZU DTG-60H. All thermal studies were conducted under an argon atmosphere with a heating rate of 10°C/min. The textural analysis was performed using a Quantachrome NOVA 2200E BET surface area and pore size analyzer, Autosorb IQ model, to obtain adsorption/desorption isotherms of the amorphous alloys $Co_{69}Nb_{23}B_8$, $Fe_{78}Si_9B_{13}$, $Co_{68}Cu_{23}B_9$ and $Fe_{64}Nb_{28}B_8$. The uniaxial compressive mechanical tests were conducted in a WDW-100 testing machine at a deformation rate of 1 10^{-4} s^{-1} at room temperature. The powder sizes of the alloys $Co_{69}Nb_{23}B_8$, $Fe_{78}Si_9B_{13}$, $Co_{68}Cu_{23}B_9$ and $Fe_{64}Nb_{28}B_8$ were pressed into cylindrical disc shapes and are 2 mm in diameter and 4 mm in height. Compression tests were performed at least in triplicate for the amorphous powders $Co_{69}Nb_{23}B_8$, $Fe_{78}Si_9B_{13}$, $Co_{68}Cu_{23}B_9$ and $Fe_{64}Nb_{28}B_8$. The magnetic properties were studied by a vibrating sample magnetometer (VSM) at room temperature of 25°C and a magnetic field in the range of ± 40 kOe. The cell viability assay by MTT for the amorphous alloys $Co_{69}Nb_{23}B_8$, $Fe_{78}Si_9B_{13}$, $Co_{68}Cu_{23}B_9$ and $Fe_{64}Nb_{28}B_8$, performed using the MTT assay with MC3T3 osteoblastic cells, showed a cytotoxic profile that, at the safe concentration, the cell viability was higher than 70%, promising potential for applicability as metallic biomaterial for biomedicine.

II. Results and discussion

Figure 1 shows the diffractograms of the alloys $Co_{69}Nb_{23}B_8$ (a), $Co_{68}Cu_{23}B_9$ (b), $Fe_{64}Nb_{28}B_8$ (c) and $Fe_{78}Si_9B_{13}$ (d) processed by mechanical grinding (HEM). In the diffractograms, in the 2θ range of 40º – 50º, a typical diffuse halo is observed, with no indication of an obvious diffraction peak corresponding to the crystalline phases, as shown in the central part inside the red dashed circle, characteristic of an amorphous structure.

Figure 2 illustrates the vibrational spectra of the amorphous alloys $Co_{69}Nb_{23}B_8$ (a), $Co_{68}Cu_{23}B_9$ (b), $Fe_{64}Nb_{28}B_8$ (c) and $Fe_{78}Si_9B_{13}$ (d) obtained by HEM in the infrared region of 4000 - 500 cm^{-1}.

The FTIR spectra of the amorphous alloy $Co_{69}Nb_{23}B_8$ (a) showed a band at ~2335.6 cm^{-1}, which is attributed to the stretching vibration modes of the C=O group of atmospheric CO_2 [26]. The FTIR absorption spectrum in the vicinity of ~2094 cm^{-1} slightly decreases in intensity, which is most likely due to the formation of some dicarbonyl $Co^{2+}(CO)_2$ species absorbing at lower frequencies [27]. The band observed at 626 cm^{-1} is attributed to the stretching frequency of Co-O, where Co is Co^{2+} and is tetrahedrally coordinated due to the presence of the spinel of Co_3O_4 [28].

Analyzing the FTIR spectrum of the amorphous alloy $Fe_{78}Si_9B_{13}$ (b) it can be observed that the absorption band observed at 2338 cm^{-1} corresponds to the presence of (R)O-H groups (R = Si and B or Ba), for example, the silanol group SiOH [29]. A broad band was observed in the region of 2104 cm^{-1} corresponding to the characteristic

stretching mode of the Si-O group [30].

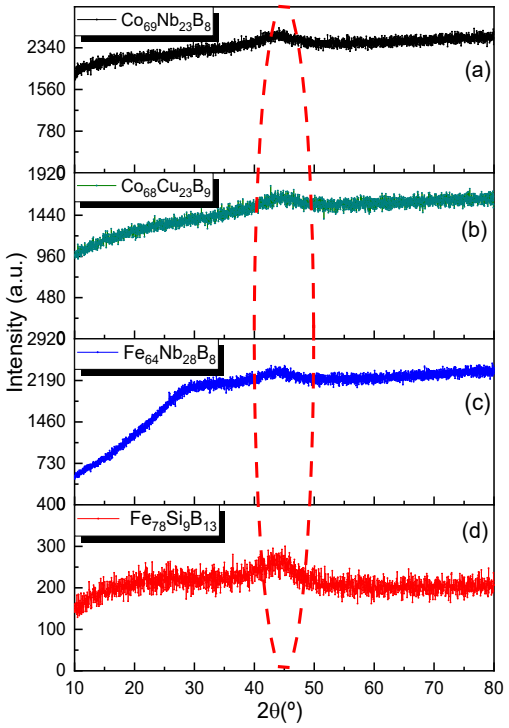

Fig. 1. X-ray diffraction patterns of the amorphous alloys $Co_{69}Nb_{23}B_8$ (a), $Co_{68}Cu_{23}B_9$ (b), $Fe_{64}Nb_{28}B_8$ (c) and $Fe_{78}Si_9B_{13}$ (d).

The band that appears around 1992 cm^{-1} corresponds to the O-Fe-O stretching mode of Fe_2O_3 [31]. The band at 638 cm^{-1} represents the stretching vibration of the Fe-O bond in Fe_3O_4 [32]. The occurrence of a band at 592 cm-1 is attributed to the stretching vibrational mode of the Si-O-Fe group [33]. The bands at 3825 cm^{-1} and 3650 cm^{-1} in the FTIR spectrum of the $Co_{68}Cu_{23}B_9$ (c) alloy are attributed to the axial stretching mode of the O-H group, due to the H_2O molecules having an incompletely developed hydrogen bond [34].

The presence of a band at 2250 cm^{-1} indicates the involvement of unstable oxidation processes of Cu(I) to Cu (II) ions, which can be attributed to vibrations caused by atmospheric CO_2 [35]. The absorption band near 2100 cm^{-1} can be ascribed to the stretching vibrations of B–O bonds in BO_3^- units, which involve the interaction of distinct oxygen groups. Furthermore, the FTIR band at 1532 cm^{-1} is attributed to a metal–metal charge transfer process associated with the oxo-bridged Co–O–Cu linkage in octahedral coordination [36].

The absorption spectra in the 1250 cm^{-1} range are attributed to the stretching of non-bridged oxygen atoms of the Co-OH type [37] Regarding the FTIR band around 2650 cm^{-1} of the amorphous alloy $Fe_{64}Nb_{28}B_8$ (d) is directly related to the presence of niobium. The nature of this band cannot be clearly established, but it may be related to the formation of P-OH···O-Nb bridges instead of P-OH···O-P [38].

This vibration becomes narrower as the niobium oxide content increases. The evolution of this band indicates that in addition to a decrease in the amount of OH, niobium oxide changes the nature of the OH bond and, therefore, the associated vibration frequency [39]. The band observed at ~2250 cm^{-1} in the $Fe_{64}Nb_{28}B_8$ alloy (d) is caused by the stretching vibration modes of the B-H group [49].

The band around 2000 cm^{-1} is attributed to the asymmetric stretching vibrations of the O-Fe-O group [41]. The FTIR spectrum showed the presence of a strong band at ~1960 cm^{-1}, being attributed to the stretching vibration mode of Nb=O [42,43]. Furthermore, the strong absorption band at 650 cm^{-1} reported in the FTIR spectrum

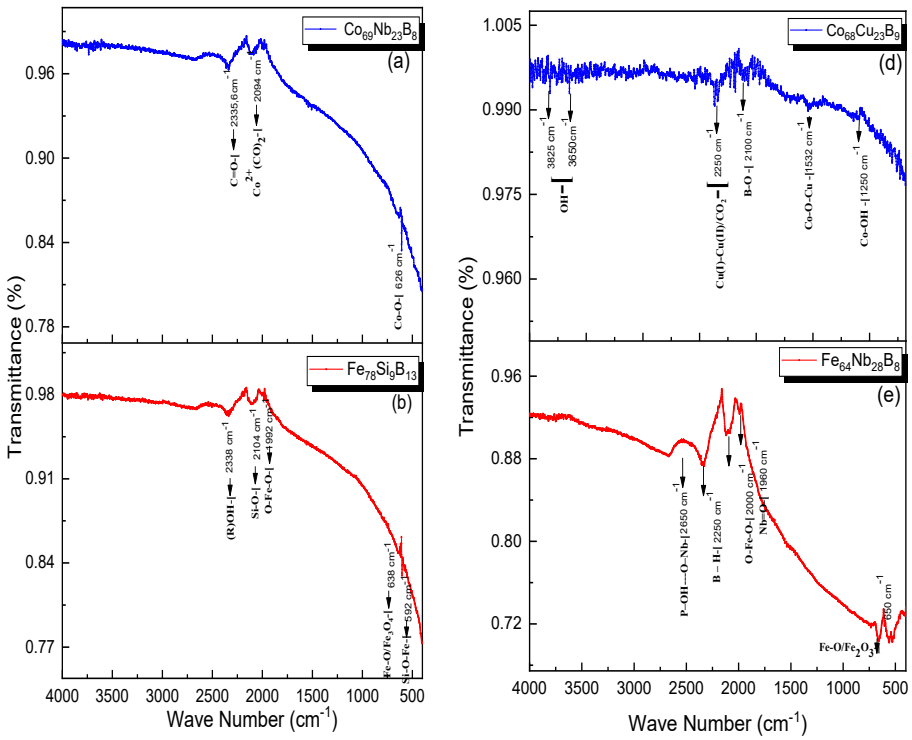

Fig. 2. FTIR spectra of the amorphous alloys $Co_{69}Nb_{23}B_8$ (a), $Co_{68}Cu_{23}B_9$ (b), $Fe_{64}Nb_{28}B_8$ (c) and $Fe_{78}Si_9B_{13}$ (d).

of the amorphous alloy is attributed to the stretching vibrations of Fe-O and Fe_2O_3 bonds [44].

All absorptions and assignments related to the amorphous alloys $Co_{69}Nb_{23}B_8$ (a), $Co_{68}Cu_{23}B_9$ (b), $Fe_{64}Nb_{28}B_8$ (c) and $Fe_{78}Si_9B_{13}$ (d) are described in Table 1.

Figure 3 illustrates the micrographs of the amorphous alloys a) $Co_{69}Nb_{23}B_8$, b) $Co_{68}Cu_{23}B_9$, c) $Fe_{78}Si_9B_{13}$ and d) $Fe_{64}Nb_{28}B_8$ obtained by SEM. The micrographs of each amorphous alloy give an idea of the morphological structure of the amorphous powders and were grouped with a scale of 50 µm and a magnification of 100kx.

In the micrograph of Figure 3 a) $Co_{69}Nb_{23}B_8$, an agglomeration of particles with irregular and very flattened morphology is observed, which occurs due to the plastic deformation and ductility of the powders that undergo hardening and bonding by crushing, resulting in final particles with irregular morphology and non-uniform size [45]. In this case, the particle size increased with irregular shape and produced a mixture with a wide particle size distribution of 50 µm [46].

The amorphous powder particles in b) $Co_{68}Cu_{23}B_9$ were milled for 15 h to reach a size of 50 µm, which shows an irregular particle morphology, typical of small flakes that transform into fine particles due to the plastic deformation of the $Co_{68}Cu_{23}B_9$ alloy powder during high-energy milling [47].

The representative SEM micrograph of the amorphous alloy c) $Fe_{78}Si_9B_{13}$ shows that the powders are

Table 1.

Wavenumber and absorption bands for the amorphous alloys $Co_{69}Nb_{23}B_8$ (a), $Co_{68}Cu_{23}B_9$ (b), $Fe_{64}Nb_{28}B_8$ (c) and $Fe_{78}Si_9B_{13}$ (d).

Amorphous alloys	Wave number (cm^{-1})	Assignment
	~2335,6	Stretching vibration modes of the C=O group of atmospheric CO_2
$Co_{69}Nb_{23}B_8$ (a)	~2094	Formation of dicarbonyl species
	~626	Attributed to the Co-O stretching frequency
	2338	Presence of (R)O-H groups (R= Si and B or Ba)
	2104	Si-O group stretching mode
$Fe_{78}Si_9B_{13}$ (b)	1992	O-Fe-O stretching mode of Fe_2O_3
	638	Stretching vibration of the Fe-O bond in Fe_3O_4 stretching
	592	Presence of stretching vibration of the Si-O-Fe group
	3825-3650	Axial stretching mode of the O-H group
	2250	Oxidation of Cu(I) ions to Cu (II) due to atmospheric CO_2
$Co_{68}Cu_{23}B_9$ (c)	2100	Stretching vibrations of the B-O bonds of BO^{3-}
	1532	Assigned to the oxo-bridge bond Co-O-Cu
	1250	Co-OH type stretching
	2650	Formation of P-OH···O-Nb bridges
	~2250	B-H group stretching vibrations
$Fe_{64}Nb_{28}B_8$ (d)	2000	Asymmetric stretching of the O-Fe-O group
	~1960	Stretching vibration of Nb=O
	650	Stretching of Fe-O and Fe_2O_3

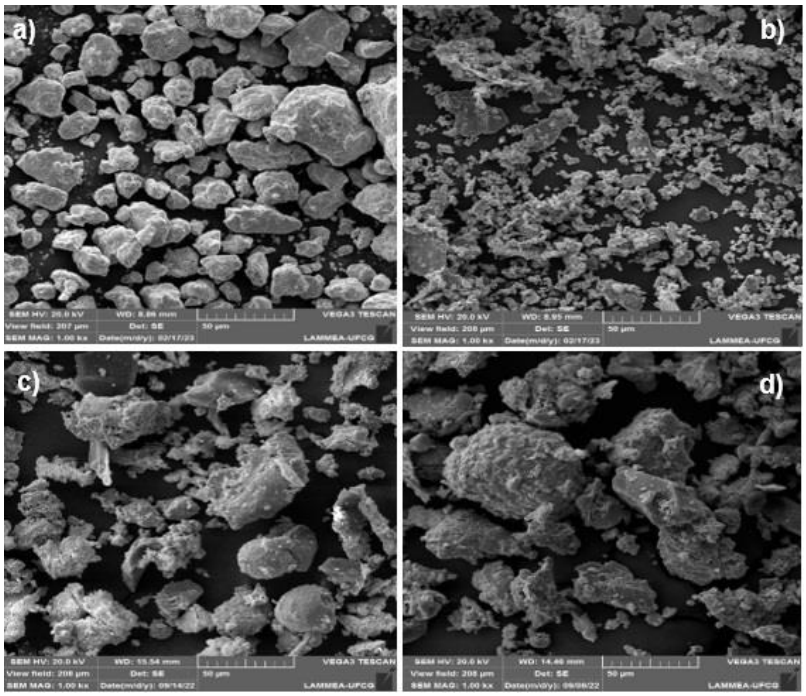

Fig. 3. Micrographs obtained by SEM of amorphous alloys a) $Co_{69}Nb_{23}B_8$, b) $Co_{68}Cu_{23}B_9$, c) $Fe_{78}Si_9B_{13}$ and d) $Fe_{64}Nb_{28}B_8$.

hardened by intense plastic deformation during grinding, becoming brittle in nature. In this case, irregular agglomeration and cold welding occur over fracturing mechanisms. Thus, the particle size is reduced and a mixture of hemispherical particles with a narrow size distribution of 50 μm is developed [48]. In this way, a more homogenized and very uniform mixture was obtained. As shown in the micrograph of the powder of the amorphous alloy d) $Fe_{64}Nb_{28}B_8$, it is clear that it presents an irregular agglomeration morphology with a uniform and homogeneous distribution, due to the numerous fractures and reduction of particles with a size of 50 μm due to the cold-welding process, presenting very few pores on its surface [49]. The balance between fracture and cold welding of powder particles is assisted by the high contact pressure between the spheres and powders, as well as between the spheres and vials, leading to the creation of new surfaces that come into contact with each other under significant plastic deformation.

This results in the flattening of the powder particles and the emergence of a varied and irregular morphology [50]. Continuous milling led to a combination of continuous fracturing and cold-welding processes, resulting in aggregates of smaller particles with irregular shapes and particle sizes of 50 μm during the 15 h of milling. Thus, it can be stated that this caused the fracture to occur more abruptly.

Figure 4 illustrates the thermal events observed from the superimposed TGA/DTA curves for the amorphous alloys $Co_{69}Nb_{23}B_8$ (a), $Co_{68}Cu_{23}B_9$ (b), $Fe_{64}Nb_{28}B_8$ (c) and $Fe_{78}Si_9B_{13}$ (d), which allows the determination of the decomposition temperatures (ºC), transformation of amorphous phases and mass losses.

In the TGA curve in Figure 4 (a) referring to the $Co_{69}Nb_{23}B_8$ alloy, the TGA curve has endothermic behavior up to a temperature of ~421°C, representing a mass loss of ~3.65%. The exothermic peak in the DTA curve, located around 406°C, is possibly associated with some crystallization or phase transformation process, or even followed by high-temperature oxidation with some mass gains [51,52]. Compared with other similar amorphous alloys, B in the alloy composition effectively increases the crystallization temperature and its thermal stability.

According to Figure 4 (a), the glass transition temperature is T_g=372.12°C and the first crystallization temperature is around T_x=406°C for the amorphous alloy $Co_{69}Nb_{23}B_8$ (a), which corresponds to the supercooled liquid region corresponding to the endothermic peak used, which is considered a good indicator of thermal stability, since the higher value of ΔT causes a delay in the nucleus, that is, $\Delta T=T_x-T_g$=33.88°C with amorphous alloys/bulk metal glasses (BMG) [53]. At higher temperatures, Co ions such as Nb are oxidized by the environment and therefore the mass can be slightly increased to 114.9% (see Figure 4 (a). It is assumed that the grain size may have increased since the ionic radius of Co (0.65Å) is larger than that of Nb (≈0.62Å) [54].

The measurements of the superimposed TGA/DTA curves of the $Fe_{78}Si_9B_{13}$ alloy in Figure 4 (b) show the DTA curve exhibiting a single exothermic peak for crystallization of the supercooled liquid at 500.13°C (T_x). In amorphous alloys or even in amorphous materials, there is a glass transition behavior prior to crystallization. In Figure 4 (b) for the $Fe_{78}Si_9B_{13}$ alloy, an endothermic peak corresponding to the glass transition of 468.59°C (T_g) and the supercooled liquid region can be observed, which is considered a good indicator of thermal stability, since a

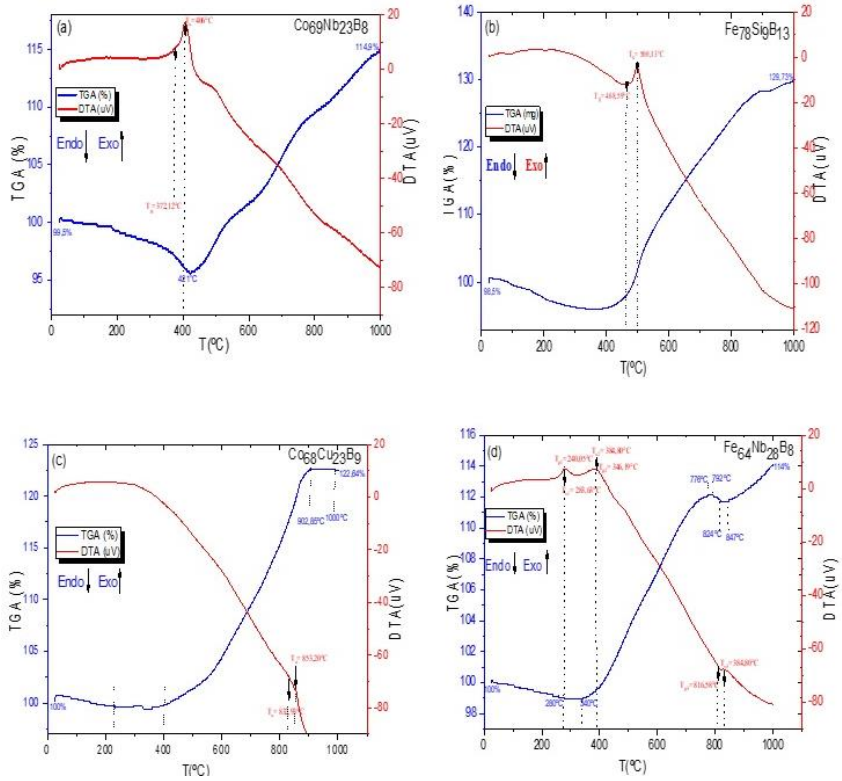

Fig. 4. Superimposed TGA/DTA curves of the amorphous alloys $Co_{69}Nb_{23}B_8$ (a), $Co_{68}Cu_{23}B_9$ (b), $Fe_{64}Nb_{28}B_8$ (c) and $Fe_{78}Si_9B_{13}$ (d).

higher value of ΔT causes a delay in nucleation, that is, $\Delta T = T_x - T_g = 31.54°C$, for amorphous alloys/bulk metallic glasses (BMG - Bulk Metallic Glasses) [55,56]. At higher temperatures, both the Fe and Si ions of the TGA are oxidized by the environment, so that the mass easily increases to 129.73% as shown in Figure 4 (b). The increase in grain size is due to high-temperature oxidation, which led to a greater increase in the ionic radius of Fe (0.78 Å) than that of Si (≈0.26 Å) [57].

In the amorphous alloy $Co_{68}Cu_{23}B_9$ in Figure 4 (c), it is observed that at T_x=853.20°C there is a small formation of a small exothermic peak for the crystallization of the supercooled liquid, followed by a low glass transition temperature of T_g=832.93°C (almost imperceptible in the graph in Figure 4 (c). This reveals a residual increase in the amorphous phase at 850°C, due to the decrease in crystallization in this last exothermic peak [58].

The value of ΔT causes a delay in the growth of the grain nucleus, that is, $\Delta T = T_x - T_g = 20.27°C$ shows a good indicator of thermal stability, with this type of stoichiometry of the amorphous alloy $Co_{68}Cu_{23}B_9$ [59]. It is also noted that there is a reactive step at the thermal decomposition temperature that is relatively high, between 902.85°C and 1000°C, which shows good thermal stability properties indicating that the mass becomes constant in this temperature range. Co ions like Cu ions are oxidized by the environment and, therefore, there is a drastic increase in mass to 122.64% in the TGA curve of $Co_{68}Cu_{23}B_9$ as illustrated in Figure 4 (c).

Figure 4 (d) illustrates the thermal events observed from the superimposed TGA/DTA curves for the $Fe_{64}Nb_{28}B_8$ alloy, where two exothermic peaks can be observed. The first peak is caused by the crystallization of the bcc-Fe(Nb) phase, and the second peak is due to the crystallization of Fe_2B and Fe_3B phases that act as an inhomogeneous nucleation site diluted with the amorphous phase that is related to the structural relaxation that occurs just before the glass transition, resulting in a generally low characteristic temperature before the phases form [60,61].

The first and second crystallization temperatures T_{x1} and T_{x2}, which are determined by the onset of the DTA peaks, are T_{x1} = 283.63ºC and T_{x2} = 384.80ºC, which, followed by their glass transition temperatures, are T_{g1} = 240.05ºC and T_{g2} = 346.19ºC, respectively. In addition, the values of $\Delta T1 = T_{x1} - T_{g1} = 43.58°C$ and $\Delta T_2 = T_{x2} - T_{g2} = 38.61°C$ cause a delay in the grain nucleus, that is, creating thermal stability for amorphous alloys/bulk metal glasses (BMG - Bulk Metal Glasses) [62]. According to Figure 4 (d), the TGA curve has a first small high step in the first temperature range from 776 to 792ºC and in the second step, a temperature ranges between 824 and 847ºC, presenting in both a relatively high thermal decomposition. Figure 5 shows the results of the textural characterization of the amorphous alloys $Co_{69}Nb_{23}B_8$ (a), $Fe_{78}Si_9B_{13}$ (b), $Co_{68}Cu_{23}B_9$ (c) and $Fe_{64}Nb_{28}B_8$ (d) obtained by HEM by N_2 adsorption/desorption isotherms.

Thus, the amorphous alloys $Co_{69}Nb_{23}B_8$ (a), $Fe_{78}Si_9B_{13}$ (b), $Co_{68}Cu_{23}B_9$ (c) and $Fe_{64}Nb_{28}B_8$ (d) presented surface structures with an adsorption isotherm curve profile, which according to IUPAC - International Union of Pure and Applied Chemistry, fall into type V [63], suggesting a mesoporous characteristic of the materials (pore size in the range of 10–250 Å) and an ordered arrangement of pores giving it a well-ordered structure [64,64]. At the same time, analyzing the hysteresis shapes corresponding to the different pore geometries, it can be observed that these amorphous alloys are represented by type 3 (H3) hysteresis loops (formation

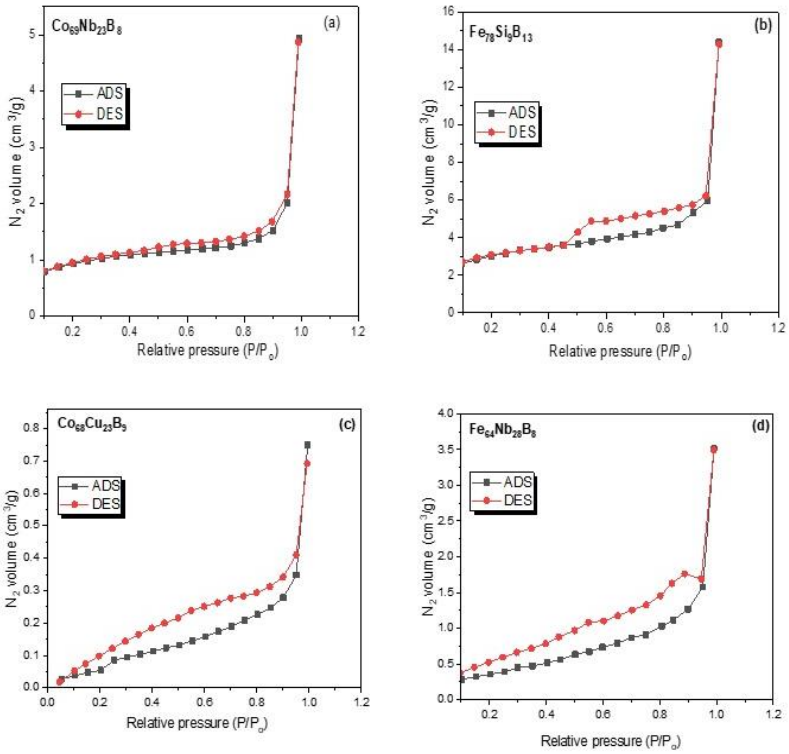

Fig. 5. N_2 adsorption/desorption isotherms for amorphous alloys $Co_{69}Nb_{23}B_8$ (a), $Fe_{78}Si_9B_{13}$ (b), $Co_{68}Cu_{23}B_9$ (c) and $Fe_{64}Nb_{28}B_8$ (d).

of wedge-shaped pores, parallel cones or plate-shaped pores) [65]. The presence of the hysteresis loop indicates that mesopores also accompany the micropores. This phenomenon has been established for activated carbons prepared under low nitrogen flow rates (500ºC) [66].

Thus, it can be concluded that these moderate carbonization conditions are a contribution to the mesopores. The pores present in these amorphous alloys are important for orthopedic biomedical applications. Based on Figure 5, typical isotherms for mesoporous solids are observed, and are characterized by a very sharp hysteresis loop between the adsorption and desorption branches for amorphous alloys.

In addition, a very significant hysteresis can appear in the adsorption and desorption branches, as they also do not return to the origin. It is observed that the absence of limitation of the adsorbed amount of N_2 is saturated at high values of P/P_o, indicating a strong tendency for a mesoporous material [66,67]. It is observed in the isotherms of amorphous alloys that the inflection point in the hysteresis occurs around P/P_o = 0.4-1, which is typically a characteristic of the existence of strong mesoporosity and an adsorption and desorption cycle. Mesoporous phases with medium and large pores were observed in the same range of P/P_o= 0.8-1 [68] in Fig. 5.

The relative pressure (P/P_o) in the separated region in the adsorption and desorption curves was greater than 0.8 in the amorphous alloys in which larger pore diameters were observed. The hysteresis was caused by the high capillary condensation that occurred in the mesopores [69]. The desorption hysteresis curve H3 contains a slope associated with a force in the hysteresis loop, due to the so-called tensile strength effect (this phenomenon perhaps occurs for N_2 at 77 K in the relative pressure range of 0.4 to 0.45). In conclusion, the isotherms of the amorphous alloys are similar to each other and present the same type IV isotherm and H3 curve of the hysteresis loop. The isotherms presented a hysteresis loop of type H3. This hysteresis typology is characteristic and normally associated with non-rigid aggregates of plate-shaped particles, originating slit pores. It is characterized by presenting different evaporation and condensation paths between the adsorption and desorption processes undergone by the adsorbent materials.

In summary, the isotherms for the amorphous alloys $Co_{69}Nb_{23}B_8$ (a), $Fe_{78}Si_9B_{13}$ (b), $Co_{68}Cu_{23}B_9$ (c) and $Fe_{64}Nb_{28}B_8$ (d are similar to each other and presented the same type IV isotherm profile and H3 hysteresis loop. The measured specific surface areas of the amorphous alloys $Co_{69}Nb_{23}B_8$ (a), $Fe_{78}Si_9B_{13}$ (b), $Co_{68}Cu_{23}B_9$ (c) and $Fe_{64}Nb_{28}B_8$ (d) are 3.215, 4.237, 3.121 and 4.201 $m^2\ g^{-1}$ respectively. These values are in good agreement with the results reported [70], when they developed new amorphous alloy catalysts of Ni–P (R–Ni–P), Ni–Co–B, and Ni–B (P)/SiO_2 type for Fischer-Tropsch process in catalytic hydrogenation reactions of various organic compounds. On the other hand, the average pore diameter values for the amorphous alloys $Co_{69}Nb_{23}B_8$ (a), $Fe_{78}Si_9B_{13}$ (b), $Co_{68}Cu_{23}B_9$ (c) and $Fe_{64}Nb_{28}B_8$ (d) were 3.16, 4.19, 3.14 and 4.18 nm, respectively, which are relatively close values compared to published works [71,72], when studying the morphological characteristics of other amorphous alloy compositions.

The mesoporous nature of these amorphous alloys obtained by HEM is confirmed by the particle volume and diameter values, which range from 2 to 50 nm according to the IUPAC classification that characterizes mesoporous materials [73,74].

Pore volume and particle size are fundamental parameters for studying the structure and porosity of these amorphous alloys, since they are related to their total area, which can serve as a reaction substrate in biomaterials. Figure 6 illustrates the behavior of magnetization (M) as a function of the applied coercive field (H) through hysteresis loops for the amorphous alloys $Co_{69}Nb_{23}B_8$ (a), $Fe_{78}Si_9B_{13}$ (b), $Co_{68}Cu_{23}B_9$ (c) and $Fe_{64}Nb_{28}B_8$ (d), which were obtained by HEM.

The M x H hysteresis loops of $Co_{69}Nb_{23}B_8$ (a), $Fe_{78}Si_9B_{13}$ (b), $Co_{68}Cu_{23}B_9$ (c) e $Fe_{64}Nb_{28}B_8$ (d) show the estimated saturation magnetizations of M_s = 15.023 emu/g, M_s = 18.932 emu/g, M_s = 15.021 emu/g and M_s = 18.832 emu/g, remanent magnetizations of M_r = 0.01603 emu/g, M_r = 0.01820 emu/g, M_r = 0.01525 emu/g and M_r = 0.01819 emu/g, and the estimated coercive fields of H_c = 70.86 kOe, H_c = 77.82 kOe, H_c = 70.14 kOe and H_c = 77.81 kOe.

In the upper part of Figure 6, it was observed that the amorphous alloys have hysteresis curves of ferrimagnetic behavior, which are characteristic of soft magnetic materials, which magnetize and demagnetize at low field values, due to their small values of remanent magnetization and coercivity, but different from zero, thus revealing the complete formation of the narrow magnetic hysteresis cycle after grinding the powder for 15 h. The remanence/saturation ratio (M_r/M_s) varied in the range of 0.000081 to 0.001066. However, the M_r/M_s ratio defines the degree of quadrature of the hysteresis loop of a magnetic material, providing information about how well the material retains its magnetization when an external magnetic field is applied and removed. It is an insightful criterion to assess the domain state, distinguishing between single domains ($M_r/M_s > 0.5$) and multidomains ($M_r/M_s \ll 0.1$) [75].

A value of $M_r/M_s \ll 0.1$ indicates that the powder particles are multidomains where the magnetization modification may be due to the domain wall motion at relatively low fields. This means that amorphous alloys produced through mechanical alloying (MA) present multidomains compared to other metallic alloy systems that are based on Bloch domain wall models and uniaxial anisotropic ferromagnetic particles that are randomly oriented with domains very close to (~0.5) [76,77]. Generally, in mechanically milled amorphous alloys, the remanence/saturation ratio (M_r/M_s) value is usually very low, between 0.001 and 0.1 [78,79]. However, on the other hand, extrinsic characteristics such as grain and/or particle size directly influence magnetic multidomains and can contribute to increased magnetization, since the larger the particle and/or grain size, the lower the energy level, favoring greater magnetization [80]. Figure 7 illustrates the typical compressive stress-strain curves for the amorphous alloys $Co_{69}Nb_{23}B_8$ (a), $Fe_{78}Si_9B_{13}$ (b), $Co_{68}Cu_{23}B_9$ (c) e $Fe_{64}Nb_{28}B_8$ (d).

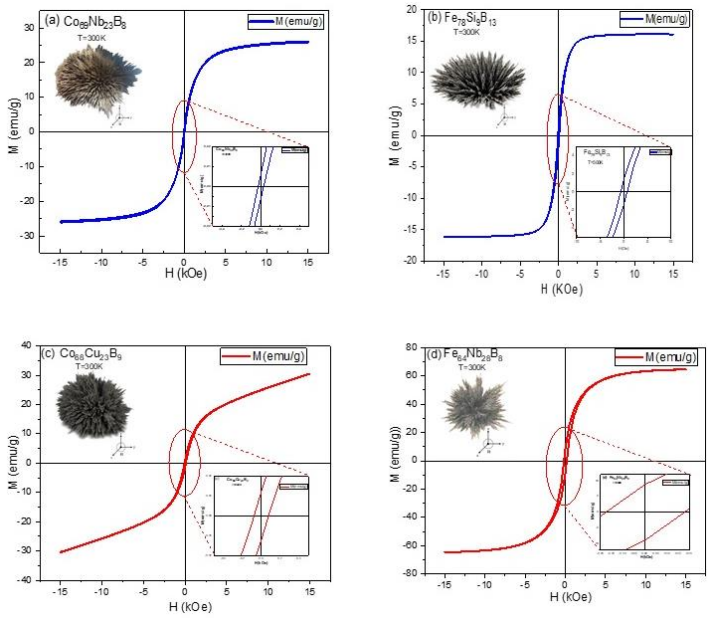

Fig. 6. M x H hysteresis curves for amorphous alloys $Co_{69}Nb_{23}B_8$ (a), $Fe_{78}Si_9B_{13}$ (b), $Co_{68}Cu_{23}B_9$ (c) e $Fe_{64}Nb_{28}B_8$ (d).

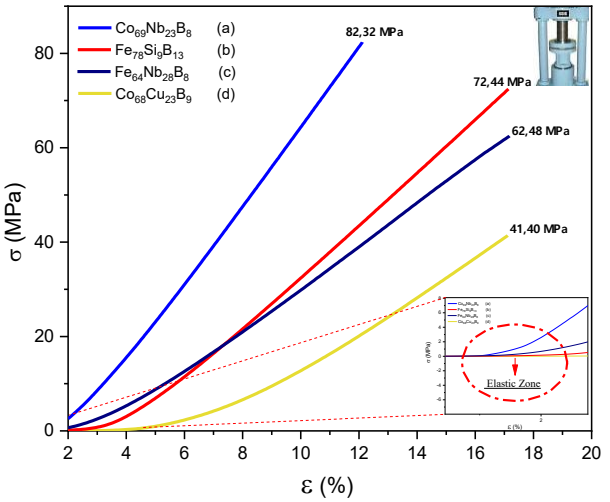

Fig. 7. Stress-strain curves of mechanical tests of compressive strength of amorphous alloys $Co_{69}Nb_{23}B_8$ (a), $Fe_{78}Si_9B_{13}$ (b), $Co_{68}Cu_{23}B_9$ (c) e $Fe_{64}Nb_{28}B_8$ (d).

The amorphous alloy $Co_{69}Nb_{23}B_8$ (a) as ground by mechanical grinding (HEM) exhibits a moderate elastic modulus of 6.80 MPa and a high yield strength of 82.37 MPa. The elastic modulus of the $Fe_{78}Si_9B_{13}$ alloy (b) was 4.23 MPa and the yield strength was slightly higher at 72.44 MPa than that of the $Co_{69}Nb_{23}B_8$ alloy (a). The $Co_{68}Cu_{23}B_9$ alloy (d) has a very low elastic modulus of 2.42 MPa and yield strength of 41.40 MPa compared to other alloys.

It is found that the amorphous alloy $Fe_{64}Nb_{28}B_8$ (c) exhibits a moderate elastic modulus. The amorphous alloys studied here, $Co_{69}Nb_{23}B_8$ (a), $Fe_{78}Si_9B_{13}$ (b), $Co_{68}Cu_{23}B_9$ (c) e $Fe_{64}Nb_{28}B_8$ (d) did not show any fracture as can be observed after the elastic deformation stage of the curve measured at the strain rate of 1 10^{-4} s^{-1} at room temperature [80]. In the right corner inside the red circle, an increase in force is observed that corresponds to the linear elastic deformation zone of the material (slope of the linear elastic zone) during the initial compression phase of each alloy [81].

It should be noted that high elastic moduli correspond to materials with more pronounced elasticity. Although a test was performed for each amorphous alloy, only the best value for each composition was reported, since the lack of tension and friction homogeneity between the sample surface and the machine plates, due to imperfect plane parallelism in small samples, did not drastically alter the stress-strain response during the test. The compressive strength value of $Co_{69}Nb_{23}B_8$ (a) is twice that of the $Co_{68}Cu_{23}B_9$ alloy (d), but it is observed. Note that the $Co_{69}Nb_{23}B_8$ alloy (a) has a lower deformation than the $Fe_{78}Si_9B_{13}$ alloy (b). In fact, these values indicate that the $Co_{69}Nb_{23}B_8$ alloy (a) is more resistant to mechanical stress and has a lower deformation capacity compared to $Fe_{78}Si_9B_{13}$ (b), but in general it can be said that all amorphous alloys have good properties and are innovative materials and are being considered for biomedical applications due to their peculiar atomic structure in terms of amorphous phase and chemical composition.

In addition, amorphous alloys based on Co and Fe have excellent mechanical properties and corrosion resistance, which are directly related to cytocompatibility and biocompatibility for biomedical applications. Therefore, they can be directly applied in future studies, such as *in vitro* cellular studies, antimicrobial properties and *in vivo* studies in animals, such as in the area of human orthopedics and bone regeneration [82].

Although the compressive strength test was performed under the same conditions, only the best value of each alloy is provided here and, depending on the application, we can say that both amorphous alloys have better properties and can be applied in metallic biomaterial [83]. It is also observed that the amorphous alloy $Fe_{64}Nb_{28}B_8$ (d) has a greater deformation, reaching twice, when compared to $Co_{68}Cu_{23}B_9$ (c) [84]. This indicates that the sample $Fe_{64}Nb_2B_8$ (d) has a compressive strength that

is twice that of the other alloy $Co_{68}Cu_{23}B_9$ (c). In practical terms, the sample $Fe_{64}Nb_{28}B_8$ (d) resists more stress and also has a greater deformation capacity when compared to $Co_{68}Cu_{23}B_9$ (c), but, depending on the application, they are said to have analogous properties [85]. Experimental results show that amorphous alloys based on Co and Fe obtained from the conventional milling process (HEM) present high elastic deformation and do not fracture [86]. These results indicate that the B and Si contents improve the resistance to deformation, therefore, the compression of these alloys is higher [87].

Figure 8 Illustrated the data obtained in the MTT cell viability test for samples F1-$Co_{69}Nb_{23}B_8$, F2-$Fe_{78}Si_9B_{13}$, G1-$Co_{68}Cu_{23}B_9$ and G2-$Fe_{64}Nb_{28}B_8$.

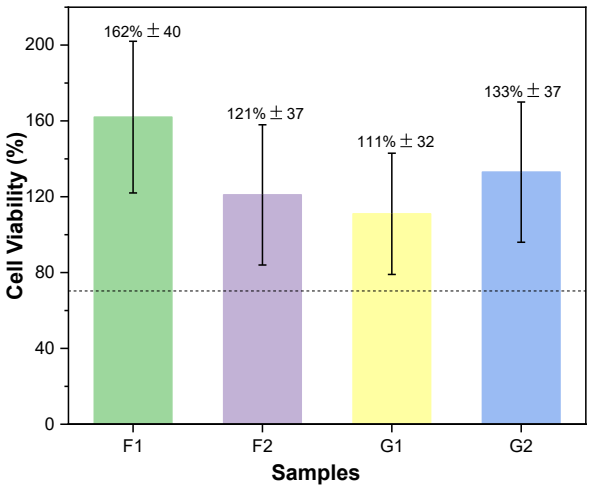

Fig. 8. Cell viability of each sample (F1–$Co_{69}Nb_{23}B_8$, F2–$Fe_{78}Si_9B_{13}$, G1–$Co_{68}Cu_{23}B_9$, G2–$Fe_{64}Nb_{28}B_8$), with the dotted line at 70% representing the ISO 10993-5 threshold for non-cytotoxicity.

It can be seen that the samples presented cell viability above 70% as specified in the BS EN ISO 10993-5:2009 standard, although their variability is high and the minimum value is slightly below that specified, with emphasis on the samples decoded as F1-$Co_{69}Nb_{23}B_8$ and G2-$Fe_{64}Nb_{28}B_8$, which were those with the highest cell viability, respectively.

However, all of them showed signs of having promising potential for applicability as metallic biomaterial for bone tissue regeneration and temporary implants for orthopedics. Based on the statistical analysis of the results obtained by the ANOVA test applied to the cell viability data of samples F1-$Co_{69}Nb_{23}B_8$, F2-$Fe_{78}Si_9B_{13}$, G1-$Co_{68}Cu_{23}B_9$ and G2-$Fe_{64}Nb_{28}B_8$, we can infer that the calculated F statistic was approximately 0.100, while the associated p-value was approximately 0.956. This indicates that the F statistic is very low compared to the critical value of the F distribution for a significance level of 0.05, and the p-value is greater than the chosen significance level. Therefore, there is insufficient statistical evidence to reject the null hypothesis that the cell viability means of the groups F1-$Co_{69}Nb_{23}B_8$, F2-$Fe_{78}Si_9B_{13}$, G1-$Co_{68}Cu_{23}B_9$ and G2-$Fe_{64}Nb_{28}B_8$ are equal.

When we look at the distribution of variation in the data, we see that most of the variability is within groups (SSE = 17528.5), while the variability between groups is relatively low (SSG = 1317.375). This is consistent with the low F-statistic observed. The between-group degrees of freedom (df_between) are 3, indicating that we are comparing the means of three different groups, while the within-group degrees of freedom (df_within) are 4, indicating that the amount of data within each group is being considered.

The between-group (MSB) and within-group (MSW) mean squares assess the variability between and within groups, respectively. With MSB around 439.125 and MSW around 4382.125, the F-ratio close to 0.1 indicates that the variability between groups is lower than that within groups. Thus, there is no significant difference between the means of groups F1-$Co_{69}Nb_{23}B_8$, F2-$Fe_{78}Si_9B_{13}$, G1-$Co_{68}Cu_{23}B_9$ and G2-$Fe_{64}Nb_{28}B_8$. It is concluded that the different titanium alloys did not have a significant impact on cell viability according to the data and methodology used.

As expected, and widely disseminated in the literature, the cytocompatibility of metal alloys, such results demonstrate, is in agreement with studies by Thanka Rajan *et al.* (2019) in which the viability of SaOS-2 cells was validated, which was greater than 100% for all dilutions, even at the 100% concentration of extracts coated with TFMG. The control (uncoated Ti6Al4V) showed lower viability than the specimen coated with TFMG [88].

In contrast, when compared with a study in which, despite the sample not being considered cytotoxic, only 78% cell viability was observed, and even after 48h of cell culture [89]. A new decrease in the proliferation rate (73%) is recorded after 72h. This suggests that the cells appeared to be very sensitive on the surface of $Zr_{37}Co_{34}Cu_{20}Ti_9$ MG and require more time to record a constant increase in the number of viable cells [90].

In this regard, that corrosive species within the human physiological environment activate the thermodynamic corrosion tendencies of metallic materials [91,92]. Depending on the toxic nature of the released cations, several biological factors can be activated, which introduce inflammatory cascades and cell apoptosis. In this context, the new amorphous titanium-based alloy $Ti_{44}Zr_{10}Pd_{10}Cu_{6+x}Co_{23-x}Ta_7$ (x = 0, 4, 8) showed biocompatibility characteristics with osteoblast-like cells (SaOS-2) that demonstrated excellent results for potential development of biomedical applications [93].

For comparison and example, evaluated the amorphous alloy based on Mg-Zn-Ca synthesized by mechanical grinding and used the MTT assay with MC3T3 osteoblastic cells and showed that the amorphous powder extract $Mg_{60}Zn_{35}Ca_5$ presented low cytotoxicity in relation to the MC3T3 cells tested, demonstrating great application as a promising biomaterial in orthopedic implants [94].

On the other hand, found in the release of metal ions such as Zn^{2+} and Mg^{2+} the induction of angiogenesis and cell proliferation, in addition to attenuated pro-inflammatory responses, which suggests a significant viability for such in the extracts studied with the release of ions that are conducive to the induction and viability of cell growth [95-100].

Although the results mentioned above in this thesis demonstrate that cell viability was around 70%, as

specified in the BS EN ISO 10993-5:2009 standard, presenting it as a promising metallic biomaterial with potential for bone tissue regeneration and temporary orthopedic implants. This result can be corroborated by the studies when they characterized crystallized and relaxed amorphous Mg-Zn-Ca alloy tapes for application in bone regeneration, as well as in the biomedical orthopedics area [101-103].

The Materials and Methods should be described with sufficient details to allow others to replicate and build on the published results. Please note that the publication of your manuscript implicates that you must make all materials, data, computer code, and protocols associated with the publication available to readers. Please disclose at the submission stage any restrictions on the availability of materials or information. New methods and protocols should be described in detail while well-established methods can be briefly described and appropriately cited.

Conclusions

Through the high-energy milling (HEM) technique, it was possible to obtain amorphous powders of the alloys $Co_{69}Nb_{23}B_8$, $Fe_{78}Si_9B_{13}$, $Co_{68}Cu_{23}B_9$, and $Fe_{64}Nb_{28}B_8$ after 15 h of milling, demonstrating their potential as metallic biomaterials for bone tissue regeneration and biomedical orthopedic applications. XRD results confirmed the successful production of fully amorphous structures, while FTIR spectra revealed characteristic vibrational bands associated with the functional groups present in the studied alloys. Complementarily, SEM micrographs showed particle agglomeration with irregular morphologies and sizes both above and below 50 µm, supporting the structural complexity of the amorphous state.

Thermal analysis further reinforced these findings, as the superimposed TGA/DTA curves exhibited a pronounced mass increase, likely associated with the oxidation of transition metal ions (Co, Nb, Fe, Cu, and Si) upon heating, leading to phase transformations. In parallel, textural analysis revealed type IV isotherm profiles with type H3 hysteresis loops, suggesting a mesoporous nature. These characteristics were consistent with the observed hysteresis curves, which displayed behavior typical of ferromagnetic materials, evidencing soft magnetic properties relevant to biomedical applications.

Mechanical testing provided additional support for their potential use, as the stress–strain curves obtained under compression confirmed good resistance to deformation. Finally, cytotoxicity assays demonstrated that the amorphous alloys $Co_{69}Nb_{23}B_8$, $Fe_{78}Si_9B_{13}$, $Co_{68}Cu_{23}B_9$, and $Fe_{64}Nb_{28}B_8$ exhibited no toxic effects on cells. In particular, the Co- and Fe-based alloys showed excellent in vitro biocompatibility, as specified by BS EN ISO 10993-5:2009, confirming their promise as metallic biomaterials for bone tissue regeneration and temporary orthopedic implants.

Author Contributions: *Conceptualization, L.N.; Methodology, L.N; Validation, L.N., and A.C.F.d.M.C.; Formal analysis, L.N.; Investigation, L.N.; Resources, L.N. and A.C.F.d.M.C.; Data curation, L.N. and A.C.F.d.M.C.; Writing—original draft, L.N.; Writing—review & editing, L.N. and A.C.F.d.M.C.; Visualization, L.N. and A.C.F.d.M.C.; Supervision, A.C.F.d.M.C.; Project administration, A.C.F.d.M.C.; Funding acquisition, A.C.F.d.M.C. All authors have read and agreed to the published version of the manuscript.*

Funding: *We would like to thank the Coordination for the Improvement of Higher Education Personnel (CAPES).*

Institutional Review Board Statement: *Not applicable.*

Informed Consent Statement: *Not applicable.*

Data Availability Statement: *Data are contained within the article.*

Acknowledgments: *The Brazilian Metallurgy and Mining Company (CBMM), the Magnetic Testing Laboratory (UAF/UFCG), the Northeast Biomaterials Evaluation and Development Laboratory (CERTBIO-UFCG), the Materials Characterization Laboratory and the Mechanical Engineering Laboratory (LEM-UFCG) and for their technical support and infrastructure.*

Conflicts of Interest: *The authors declare no conflict of interest.*

Luciano Nascimento – Doctor and Researcher in materials science and engineering.
Ana Cristina Figueiredo de Melo Costa – Doctor of in materials science and engineering, Associate Professor.

[1] M.A. Abid, D.A. Abid, W.J. Aziz, T.M. Rashid, *Iron oxide nanoparticles synthesized using garlic and onion peel extracts rapidly degrade methylene blue dye*. Physica B: Condensed Matter, 622, 413277 (2021); https://doi.org/10.1016/j.physb.2021.413277.

[2] B. Adejuyigbe, J. Kallini, D. Chiou, J.R. Kallini, *Osteoporosis: molecular pathology, diagnostics, and therapeutics.* International Journal of Molecular Sciences, 24(19), 14583 (2023); https://doi.org/10.3390/ijms241914583.

[3] R. Adelfar, H. Mirzadeh, A. Ataie, M. Malekan, *Crystallization kinetics of mechanically alloyed amorphous Fe-Ti alloys during annealing*. Advanced Powder Technology 31(8), 3215 (2020); https://doi.org/10.1016/j.apt.2020.06.006.

[4] F. Ahangaran, A. Hassanzadeh, S. Nouri, *Surface modification of Fe_3O_4@SiO_2 microsphere by silane coupling agent*. International Nano Letters 3, 1 (2013); https://doi.org/10.1186/2228-5326-3-23.

[5] M. Ahmad, J. Chen, K. Yang, T. Shah, Q. Zhang, B. Zhang, *Preparation of amidoxime modified porous organic polymer flowers for selective uranium recovery from seawater.* Chemical Engineering Journal, 418, 129370 (2021); https://doi.org/10.1016/j.cej.2021.129370.

[6] Z.A. Alothman, *A review: fundamental aspects of silicate mesoporous materials*. Materials, 5(12), 2874 (2012); https://doi.org/10.3390/ma5122874.

[7] S. An, Q. Gong, Y. Huang, *Promotive Effect of Zinc Ions on the Vitality, Migration, and Osteogenic Differentiation of Human Dental Pulp Cells*. Biological Trace Element Research, 175(1), 112 (2017); https://doi.org/10.1007/s12011-016-0763-7.

[8] Z.Y. An, Y.H. Zhang, X. Li, Y. Gu, *Magnetic and thermal characterization of Fe-B-P amorphous nanoparticles prepared by chemical reduction*. Journal of Magnetism and Magnetic Materials 560, 169648 (2022); https://doi.org/10.1016/j.jmmm.2022.169648.

[9] B. Avar, S. Ozcan, *Characterization and amorphous phase formation of mechanically alloyed $Co_{66}Fe_5Ni_5Ti_{25}B_5$ powders*. Journal of Alloys and Compounds 650, 53 (2015); https://doi.org/10.1016/j.jallcom.2015.07.268.

[10] G. Bai, H. Dong, Z. Zhao, Y. Wang, Q. Chen, M. Qiu, *Preparation of nanoscale Ni–B amorphous alloys and their application in the Selective Hydrogenation of Cinnamic Acid*. Journal of Nanoscience and Nanotechnology 13(7), 5012 (2013); https://doi.org/10.1166/jnn.2013.7572.

[11] R.T. Beck, K.D. Illingworth, K.J. Saleh, *Review of periprosthetic osteolysis in total joint arthroplasty: an emphasis on host factors and future directions*. Journal of Orthopaedic Research 30 (4), 541 (2012); https://doi.org/10.1002/jor.21554.

[12] M. Beldjehem, S. Alleg, N. Bensebaa, J.J. Suñol, J.M. Greneche, *Thermal Stability, Structure, Hyperfine, and Magnetic Properties of Nanostructured FeCo-2.5 wt.% Ni Powders.* Journal of Superconductivity and Novel Magnetism 36(1), 301 (2023); https://doi.org/10.1007/s10948-022-06467-3.

[13] M. Belyansky, M. trenary, *Reflection adsorption infrared spectroscopy of the oxidation of thin films of boron and hafnium diboride grown on Hf (0001).* Journal of Vacuum Science & Technology A: Vacuum, Surfaces, and Films 15(6), 3065 (1997); https://doi.org/10.1116/1.580848.

[14] S. Bose, D. Ke, H. Sahasrabudhe, A. Bandyopadhyay, *Additive manufacturing of biomaterials*. Progress in Materials Science 93, 45 (2018); https://doi.org/10.1016/j.pmatsci.2017.08.003.

[15] T.C. Brunold, N. Tamura, N. Kitajima, Y. Moro-oka, E.I. Solomon, *Spectroscopic Study of [$Fe_2(O_2)$ $(OBz)_2$ {HB (pz ')$_3$}$_2$]: Nature of the μ-1,2 Peroxide− Fe (III) Bond and Its Possible Relevance to O_2 Activation by Non-Heme Iron Enzymes*. Journal of the American Chemical Society 120(23**),** 5674 (1998).

[16] L.J. Burcham, J. Datka, I.E. WACHS, *In situ vibrational spectroscopy studies of supported niobium oxide catalysts.* The Journal of Physical Chemistry B, 103(29), 6015(1999).

[17] Q. Cao, G. Huang, L. Ma, L. Xing, *Comparison of a cold-sprayed and plasma-sprayed $Fe_{25}Cr_{20}Mo_1Si$ amorphous alloy coatings on 40Cr substrates*. Materials and Corrosion 71(11), 1872 (2020); https://doi.org/10.1002/maco.202011558.

[18] T. Cheung, S.K. Bhargava, M. Hobday, K. Foger, *Adsorption of NO on Cu exchanged zeolites, an FTIR study: effects of Cu levels, NO pressure, and catalyst pretreatment*. Journal of Catalysis 158(1), 301 (1996).

[19] K. Choi, S. Omanovic, *Solution combustion synthesis of nanostructured Ni/W-containing electrocatalysts for hydrogen evolution reaction: The effect of fuel-to-oxidant ratio*. Nano-Structures & Nano-Objects 37, 101075 (2024); https://doi.org/10.1016/j.nanoso.2023.101075.

[20] K. Chong, Y. Gao, Z. Zhang, Y. Zou, X. Liang, *Thermal stability and corrosion behavior of a novel $Zr_{22.5}Ti_{22.5}Hf_{22.5}Ni_{22.5}Ta_{10}$ high-entropy amorphous alloy*. Corrosion Science 213, 110979 (2023); https://doi.org/10.1016/j.corsci.2023.110979.

[21] C. Cui, C. Ren, Y. Liu, S. Wang, H. Su, *Directional solidification of Fe-Al-Ta eutectic by electron beam floating zone melting.* Journal of Alloys and Compounds 785, 62 (2019); https://doi.org/10.1016/j.jallcom.2019.01.158.

[22] M.K. Datta, D.T. Chou, D. Hong, P. Saha, S.J. Chung, B. Lee, A. Sirinterlikci, M. Ramanathan, A. Roy, P.N. Kumta, *Structure and thermal stability of biodegradable Mg–Zn–Ca based amorphous alloys synthesized by mechanical alloying*. Materials Science and Engineering: B: 176(20), 1637 (2011); https://doi.org/10.1016/j.mseb.2011.08.008.

[23] J.F. Deng, H. Li, W. Wang*, Progress in design of new amorphous alloy catalysts.* Catalysis today 51(1), 113 (1999).

[24] B. Dong, S. Zhou, S. Pan, Y. Wang, J. Qin, Y. Xing, *Relationship between relaxation embrittlement and atomic cluster structure in amorphous alloys.* Journal of Non-Crystalline Solids 626, 122770 (2024); https://doi.org/10.1016/j.jnoncrysol.2023.122770.

[25] M.H.K. Feizabad, G.R. Khayati, S. SharafI, M. Ranjbar, *Improvement of soft magnetic properties of $Fe_{0.7}Nb_{0.1}Zr_{0.1}T_{i0.1}$ amorphous alloy: A kinetic study approach.* Journal of Non-Crystalline Solids 493, 11 (2018); https://doi.org/10.1016/j.jnoncrysol.2018.04.033.

[26] M. Füredi, C.V. Manzano, A. Marton, B. Fodor, A. Alvarez-fernandez, S. Guldin, *Beyond the meso/macroporous boundary: extending capillary condensation-based pore size characterization in thin films through tailored Adsorptives*. The Journal of Physical Chemistry Letters 15(5), 1420 (2024); https://doi.org/0.1021/acs.jpclett.3c03442.

[27] B.N. Galimzyanov, A.V. Mokshin, *Mechanical response of mesoporous amorphous NiTi alloy to external deformations*. International Journal of Solids and Structures 224, 111047 (2021); https://doi.org/10.1016/j.ijsolstr.2021.111047.

[28] V.A. Georgeanu, O. Gingu, I.V. Antoniac, H.O. Manolea, *Current options and future perspectives on bone graft and biomaterials substitutes for bone repair, from clinical needs to advanced biomaterials research.* Applied Sciences 13(14), 8471 (2023); https://doi.org/10.3390/app13148471.

[29] O. Güler, T. Varol, Ü. Alver, A. Çanakçi, *The effect of flake-like morphology on the coating properties of silver coated copper particles fabricated by electroless plating*. Journal of Alloys and Compounds 782, 679 (2019); https://doi.org/10.1016/j.jallcom.2018.12.229.

[30] X.X. Guo, T.T. Hu, B. Meng, Y. Sun, Y. F. Han, *Catalytic degradation of anthraquinones-containing H_2O_2 production effluent over layered Co-Cu hydroxides: defects facilitating hydroxyl radical generation*. Applied Catalysis B: Environmental 260, 118157 (2020); https://doi.org/10.1016/j.apcatb.2019.118157.

[31] K.I. Hadjiivanov, D.A. Panayotov, M.Y. Mihaylov, E.Z. Ivanova, K.K. Chakarova, S. M. Andonova, N. L. Drenchev, Power of infrared and raman spectroscopies to characterize metal-organic frameworks and investigate their interaction with guest molecules. Chemical Reviews 121(3), 1286 (2020); https://doi.org/10.1021/acs.chemrev.0c00487.

[32] K. Hadjiivanov, B. Tsyntsarski, T. Venkov, D. Klissurski, M. Daturi, J. Saussey, J.C. Lavalley, *FTIR spectroscopic study of CO adsorption on Co–ZSM-5: Evidence of formation of $Co^{+}(CO)_4$ species.* Physical Chemistry Chemical Physics 5(8), 1695 (2003); https://doi.org/10.1039/b300844d.

[33] A. Houssou, S. Amirat, H. Ferkous, S. Alleg, K. Dadda, R. Boulechfar, A. Erto, N. Elboughdiri, K.K. Yadav, M.A. Alreshidi, J.K. Bhutto, W. Bouchelaghem, L. Abadlia, Y. Benguerba, *Experimental and computational investigations on mechanically alloyed $Fe_{55}Co_{30}Ni_{15}$ powders.* Powder Technology, 119203 (2023); https://doi.org/10.1016/j.powtec.2023.119203.

[34] L.J. Huang; H.J. Lin,; H. Wang, L.Z. Ouyang, M. Zhu, *Amorphous alloys for hydrogen storage*. Journal of Alloys and Compounds 941, 168945 (2023); https://doi.org/10.1016/j.jallcom.2023.168945.

[35] S.J. Huang, A. Muneeb, A. Abbas, R. Sankar, The effect of Mg content and milling time on the solid solubility and microstructure of Ti–Mg alloys processed by mechanical milling. Journal of Materials Research and Technology 11, 1424 (2021); https://doi.org/https://doi.org/10.1016/j.jmrt.2021.01.097.

[36] F.S. Irwansyah, A.I. Amal, E.W. Diyanthi, E.P. Hadisantoso, A. R. Noviyanti, D. R. Eddy, R. Risdiana, *How to read and determine the specific surface area of inorganic materials using the Brunauer-Emmett-Teller (BET) method*. ASEAN Journal of Science and Engineering 4(1), 61 (2024); https://doi.org/10.17509/ajse.v4i1.60748.

[37] ISO 10993-5:2009 *Biological evaluation of medical devices Part* 5: Tests for in vitro cytotoxicity. ISO Standards (2009).

[38] ISO. *Biological evaluation of medical devices. Tests for in vitro cytotoxicity.:* International Organization for Standardization, BS EN ISO 10993-5 (2009).

[39] A. Jabed, Z.U. Rahman, M.M. Khan, W. Haider, I. Shabib, *Combinatorial development and in vitro characterization of the quaternary Zr–Ti–X–Y (X–Y= Cu–Ag/Co–Ni) metallic glass for prospective bioimplants*. Advanced Engineering Materials 21(12), 1900726 (2019); https://doi.org/10.1002/adem.201900726.

[40] B. Jeż, M. Nabiałek, K.J. Jeż, *Preparation of Magnetic Composites Based on Bulk Amorphous Iron Alloys*. Materiale Plastice 56(4), 1008 (2019); https://doi.org/10.37358/MP.19.4.5299.

[41] K. Kaneko, H. Otsuka, *New IUPAC recommendation and characterization of nanoporous materials with physical adsorption.* Accounts of Materials & Surface Research 5(2), 25 (2020).

[42] N. Khitouni, B. Hammami; N. Llorca-Isern, W. B. Mbarek, J. J. SUÑOL, M. Khitouni, *Microstructure and Magnetic Properties of Nanocrystalline $Fe_{60-x}Co_{25}Ni_{15}S_{ix}$ Alloy Elaborated by High-Energy Mechanical Milling*. Materials 15 (18), 6483 (2022); https://doi.org/10.3390/ma15186483.

[43] G.L. Koons, M. Diba, A. G. Mikos, *Materials design for bone-tissue engineering*. Nature Reviews Materials 5(8), 584 (2020); https://doi.org/10.1038/s41578-020-0204-2.

[44] P.S. KowalskI, C. Bhattacharya, S. Afewerki, R. Langer, *Smart biomaterials: recent advances and future directions*. ACS Biomaterials Science & Engineering 4(11), 3809 (2018); https://doi.org/10.1021/acsbiomaterials.8b00889.

[45] J.D. Lamplot, B.L. Smith, H.S. Slone, O.L. Hauck, C. A. Wijdicks, *Tape-reinforced graft suturing and retensioning of adjustable-loop cortical buttons improve quadriceps tendon autograft biomechanics in anterior cruciate ligament reconstruction: A cadaveric study. Arthroscopy:* The Journal of Arthroscopic & Related Surgery 40(1), 136 (2024); https://doi.org/10.1016/j.arthro.2023.06.021.

[46] J. D. Lee, Química inorgânica Não Tão Concisa. São Paulo: Editora Blücher, 544 (1999).

[47] T. Lee, M. Yamasaki, Y. Kawamura, Y. Lee, C.S. Lee, *High strain-rate superplasticity of AZ91 alloy achieved by rapidly solidified flaky powder metallurgy*. Materials Letters 234, 245 (2019); https://doi.org/10.1016/j.matlet.2018.09.090.

[48] R. Li, Q. Chen, L. Ji, X. Peng, G. Huang, *Based on internal friction theory: Investigating of Fe-based bulk amorphous alloys on mechanical properties with different Si content*. Journal of Non-Crystalline Solids 563, 120813 (2021).

[49] K. Liu, S. Wang, Y. Feng, K. Zhang, Y. Zhang, *Phase transformation mechanism and magnetic properties of Sm-Fe alloys produced by melt-spinning and high-energy ball milling*. Journal of Magnetism and Magnetic Materials 513, 167229 (2020); https://doi.org/10.1016/j.jmmm.2020.167229.

[50] L. Liu, Y. Ahmadi, K.H. Kim, D. Kukkar, J.E. Szulejko, *The relative dominance of surface oxygen content over pore properties in controlling adsorption and retrograde behavior of gaseous toluene over microporous carbon*. Science of The Total Environment 906, 167308 (2024); https://doi.org/10.1016/j.scitotenv.2023.167308.

[51] N. Liu, Y. Gao, C. Chen, P. Zhou, X. Wang, J. Zhang, J. CAO, *Oxidation behavior of $Al_{15}Fe_{20}Co_{20}Ni_{20}Cr2_{5-x}Nb_x$ high-entropy alloys at elevated temperatures.* Vacuum 213, 112092 (2023); https://doi.org/10.1016/j.vacuum.2023.112092.

[52] S. Liu, I. Shohji, T. Kobayashi, J. Hirohashi, T. Wake, H. Yamamoto, Y. Kamakoshi, *Mechanistic study of Ni–Cr–P alloy electrodeposition and characterization of deposits*. Journal of Electroanalytical Chemistry 897, 115582 (2021); https://doi.org/10.1016/j.jelechem.2021.115582.

[53] X. Liu, X. Wang, Y. Si, F. Han, *Glass-Forming Ability and Thermal Properties of $Al_{70}Fe_{12.5}V_{12.5}X_5$ (X= Zr, Nb, Ni) Amorphous Alloys via Minor Alloying Additions*. Nanomaterials 11(2), 488 (2021); https://doi.org/10.3390/nano11020488.

[54] J.A. Lopez, F. González, F.A. Bonilla, G. Zambrano, M.E. Gómez, *Synthesis and characterization of Fe_3O_4 magnetic nanofluid*. Revista Latinoamericana de Metalurgia y Materiales 30(1), 60 (2010).

[55] J. Málek, *Structural relaxation rate and aging in amorphous solids*. The Journal of Physical Chemistry C:127(12), 6080 (2023); https://doi.org/10.1021/acs.jpcc.3c00637.

[56] J. Manoj, R. E. Vizhi, Effect of Al substitution on their structural and magnetic properties of $Ba_{0.5}Sr_{0.5}Fe_{12}O_{19}$ prepared via sol–gel auto-combustion method. Journal of Materials Science: Materials in Electronics 35(6), 370 (2024); https://doi.org/10.1007/s10854-024-12037-1.

[57] M. Monavarian, S. Kader, S. Moeinzadeh, E. Jabbari, *Regenerative scar-free skin wound healing*. Tissue Engineering Part B: Reviews 25(4), 294 (2019); https://doi.org/10.1089/ten.TEB.2018.0350.

[58] M. Moneta, M. Wasiak, P. Sovak, *Temperature dependence of structural and magnetic transformations in Finemet-type amorphous alloys with Fe substituted for La*. Journal of Thermal Analysis and Calorimetry148(4), 1577 (2023); https://doi.org/10.1007/s10973-022-11675-z.

[59] A. Monfared, A. Ghaee, S. Ebrahimi-Barough, *Preparation and characterization of crystallized and relaxed amorphous Mg-Zn-Ca alloy ribbons for nerve regeneration application*. Journal of Non-Crystalline Solids 489, 71 (2018); https://doi.org/10.1016/j.jnoncrysol.2018.03.031.

[60] S.M. Moosavinejad, M. Madhoushi, M. VakilI, D. Rasouli, *Evaluation of degradation in chemical compounds of wood in historical buildings using FT-IR and FT-Raman vibrational spectroscopy*. Maderas. Ciencia y Tecnología 21(3), 381 (2019); http://dx.doi.org/10.4067/S0718-221X2019005000310.

[61] Z. Msetra, N. Khitouni, A. Alsawi, M. Khitouni, V. Optasanu, J.J. Suñol, M. Chemingui, *Structural, microstructural, and magnetic properties of nanocrystalline-amorphous Fe–Co–Ta–B alloy processed by high-energy mechanical alloying*. Journal of Materials Research and Technology 26, 8934 (2023); https://doi.org/10.1016/j.jmrt.2023.09.183.

[62] A. Mukhtar, N. Mellon, S. Saqib, L. S. Pee, M.A. Bustam, *Extension of BET theory to CO_2 adsorption isotherms for ultra-microporosity of covalent organic polymers.* SN Applied Sciences 2(7), 1 (2020); https://doi.org/10.1007/s42452-020-2968-9.

[63] N.J. Murphy, D. Graan, G.D. Briggs, Z.J. Balogh, *Acute minimally invasive bone grafting of long bone fractures to reduce the incidence of fracture non-union.* Medical Hypotheses 178, 111131 (2023); https://doi.org/10.1016/j.mehy.2023.111131.

[64] P. Murugaiyan, A. Mitra, R.K. Roy, A.K. Panda, *Nanocrystallization and Core-loss properties of Fe-rich FeSiBPNbCu nanocrystalline alloy.* Journal of Magnetism and Magnetic Materials 552, 169228 (2022); https://doi.org/10.1016/j.jmmm.2022.169228.

[65] N. Nwahara, G. Abrahams, J. Mack, E. Prinsloo, T. Nyokong, *A hypoxia responsive silicon phthalocyanine containing naphthoquinone axial ligands for photodynamic therapy activity*. Journal of Inorganic Biochemistry 239, 112078 (2023); https://doi.org/10.1016/j.jinorgbio.2022.112078.

[66] Y. Nykyruy, S. Mudry, Y. Kulyk, A. Borisyuk, *Magnetic properties and nanocrystallization process in Co–(Me)–Si–B amorphous ribbons*. Applied Nanoscience, 1 (2022); https://doi.org/10.1007/s13204-022-02746-6.

[67] L. Petit, T. Cardinal, J. J. Videau, E. Durand, L. Canioni, M. Martines, Y. Guyot, G. Boulon, *Effect of niobium oxide introduction on erbium luminescence in borophosphate glasses*. Optical Materials 28(3), 172 (2006); https://doi.org/10.1016/j.optmat.2004.12.007.

[68] Y. Prabhu, A. Jain, S. Vincent, W.H. Ryu, E.S. Park, R. Kumar, A.D. Bagde, J. Bhatt, *Compositional design and in vitro investigation on novel Zr–Co–Cu–Ti metallic glass for biomedical applications*. Intermetallics. 150, 107692 (2022); https://doi.org/10.1016/j.intermet.2022.107692.

[69] N.V. Priezjev, *The effect of thermal history on the atomic structure and mechanical properties of amorphous alloys*. Computational Materials Science174, 109477 (2020); https://doi.org/10.1016/j.commatsci.2019.109477.

[70] N. Primeau, C. Vautey, M. Langlet, *The effect of thermal annealing on aerosol-gel deposited SiO_2 films: a FTIR deconvolution study*. Thin Solid Films 310(1-2), 47 (1997); https://doi.org/10.1016/S0040-6090(97)00340-4.

[71] N.E. Putra, M.J. Mirzaali, I. Apachitei, J. Zhou, A.A. Zadpoor, *Multi-material additive manufacturing technologies for Ti-, Mg-, and Fe-based biomaterials for bone substitution*. Acta biomaterialia 109, 1 (2020); https://doi.org/10.1016/j.actbio.2020.03.037.

[72] S. Rajan, Thanka; A. Bendavid, B. Subramanian, *Cytocompatibility assessment of Ti-Nb-Zr-Si thin film metallic glasses with enhanced osteoblast differentiation for biomedical applications*. Colloids and Surfaces B: Biointerfaces 173, 109 (2019); https://doi.org/10.1016/j.colsurfb.2018.09.041.

[73] A. Rasouli, H. Naffakh-Moosavy, *Dissimilar laser welding of NiTi shape memory alloy to NiCr alloy*. Journal of Materials Research and Technology 26, 3947 (2023); https://doi.org/10.1016/j.jmrt.2023.08.175.

[74] A. Rathi, V.M. Meka, T.V. Jayaraman, *Synthesis of nanocrystalline equiatomic nickel-cobalt-iron alloy powders by mechanical alloying and their structural and magnetic characterization*. Journal of Magnetism and Magnetic Materials 469, 467 (2019); https://doi.org/10.1016/j.jmmm.2018.09.002.

[75] V. Rathod, A.V. Anupama, R.V. Kumar, V.M. Jali, B. Sahoo, Correlated vibrations of the tetrahedral and octahedral complexes and splitting of the absorption bands in FTIR spectra of Li-Zn ferrites. Vibrational Spectroscopy 92, 267 (2017); https://doi.org/10.1016/j.vibspec.2017.08.008.

[76] M. Roesner, S. Zankovic, A. Kovacs, M. Benner, R. Barkhoff, M. Seidenstuecker, *Mechanical Properties and Corrosion Rate of $ZnAg_3$ as a Novel Bioabsorbable Material for Osteosynthesis*. Journal of Functional Biomaterials 15 (2), 28 (2024); https://doi.org/10.3390/jfb15020028.

[77] I. Roohani, G. C. Yeo, S. M. Mithieux, A. S. Weiss, *Emerging concepts in bone repair and the premise of soft materials.* Current Opinion in Biotechnology 74, 220 (2022); https://doi.org/10.1016/j.copbio.2021.12.004.

[78] P. Sahu, S. Samal, V. Kumar, *Influence of Si and Mn on the Phase Formation, Crystallization Kinetics, and Enhanced Magnetic Properties of Mechanically Alloyed NiCoFe ($SiMn_x$ High Entropy Amorphous Alloys*. Silicon, 1 (2023); https://doi.org/10.1007/s12633-023-02324-7.

[79] P. Salwa, T. Goryczka, *Crystallization of mechanically alloyed $Ni_{50}Ti_{50}$ and $Ti_{50}Ni_{25}Cu_{25}$ shape memory alloys*. Journal of Materials Engineering and Performance 29(5), 2848 (2020); https://doi.org/10.1007/s11665-020-04820-y.

[80] D. S. Sanditov, M.I. Ojovan, M.V. Darmaev, *Glass transition criterion and plastic deformation of glass.* Physica B: Condensed Matter 582, 411914 (2020); https://doi.org/10.1016/j.physb.2019.411914.

[81] J. Serafin, B. Dziejarski, *Activated carbons—Preparation, characterization and their application in CO_2 capture: A review.* Environmental Science and Pollution Research 31(28), 40008 (2024); https://doi.org/10.1007/s11356-023-28023-9.

[82] L. Shan, X. Wang, Y. Wang, *Extension of solid solubility and structural evolution in nano-structured Cu-Cr solid solution induced by high-energy milling*. Materials 13(23), 5532 (2020); https://doi.org/10.3390/ma13235532.

[83] J.F. Shen, C.M. Wu, J.J. Yu, Y.R. Li, *Investigation on molecular cluster behavior and initiation of capillary condensation within nanoarrays*. International Journal of Heat and Mass Transfer 210, 124173 (2023); https://doi.org/10.1016/j.ijheatmasstransfer.2023.124173.

[84] X.Z. Shi, Y. Gu, T.Y. Liu, Z. H. Jiang, R. Li, F. Zeng, *Effect of different P_2O_5/SnF_2 ratios on the structure and properties of phosphate glass.* Journal of Non-Crystalline Solids 578, 121350 (2022).

[85] A. Špaldoňová, M. Havelcová, L. Lapčák, V. Machovič, D. Titěra, *Analysis of beeswax adulteration with paraffin using GC/MS, FTIR-ATR and Raman spectroscopy.* Journal of Apicultural Research 60(1), 73 (2021).

[86] C. Sun, X. Hai, S. Xi, Z. Fan, P. Li, W. Wang, *New insights of solid-state alloying and amorphous-nanocrystalline cyclic phase transitions during Cr-40 wt.% Mo powder milling.* Journal of Alloys and Compounds 731, 667 (2018); https://doi.org/10.1016/j.jallcom.2017.10.083.

[87] S. Tantavisut, B. Lohwongwatana, A. Khamkongkaeo, A. Tanavalee, P. Tangpornprasert, P. Ittiravivong, *In vitro biocompatibility of novel titanium-based amorphous alloy thin film in human osteoblast-like cells*. Chulalongkorn Medical Journal 63(2), 89 (2019); https://doi.org/10.58837/CHULA.CMJ.63.2.4.

[88] X. Tao, Z. Zhang, B. Zhang, S. Zhu, Y. Fan, H.Tian, Plasma sprayed CoNiCrMoNb (BSi) high-entropy amorphous alloy coating: The effect of spraying power on microstructure, mechanical and tribological properties. Materials Chemistry and Physics 314, 128887 (2024); https://doi.org/10.1016/j.matchemphys.2024.128887.

[89] S. Thanka Rajan, A. Bendavid, B. Subramanian, *Cytocompatibility assessment of Ti-Nb-Zr-Si thin film metallic glasses with enhanced osteoblast differentiation for biomedical applications*. Colloids and Surfaces B: Biointerfaces 173, 109 (2019); https://doi.org/10.1016/j.colsurfb.2018.09.041.

[90] Q. Tian, K. Deng, Z. Xu, K. Han, H. Zheng, *Microstructural Characterization and Mechanical Property of Al-Li Plate Produced by Centrifugal Casting Method*. Metals 11(6), 966 (2021); https://doi.org/10.3390/met11060966.

[91] Y. Tian, Q. Chen, C. Yan, H. Deng, Y. He, *Classification of adsorption isotherm curves for shale based on pore structure*. Petrophysics 61(05), 417 (2020).

[92] C.F. Toncón-Leal, J. Villarroel-Rocha, M.T.P.D. Silva, T.P. Braga, K. Sapag, *Characterization of mesoporous region by the scanning of the hysteresis loop in adsorption–desorption isotherms*. Adsorption 27(7), 1109 (2021); https://doi.org/10.1007/s10450-021-00342-8.

[93] M.M. Vasić, T. Žák, N. Pizúrová, I.S. Simatović, D.M. Minić, *Influence of Thermal Treatment on Microstructure and Corrosion Behavior of Amorphous $Fe_{40}Ni_{40}B_{12}Si_8$ Alloy*. Metallurgical and Materials Transactions A: 52, 34 (2021).

[94] C. Velmurugan, V. Senthilkumar, *The effect of Cu addition on the morphological, structural and mechanical characteristics of nanocrystalline NiTi shape memory alloys*. Journal of Alloys and Compounds 767, 944 (2018); https://doi.org/10.1016/j.jallcom.2018.07.217.

[95] J.L. Wang, Y. Wan, Z.J. Ma, Y.C. Guo, Z. Yang, P. Wang, J.P. Li, *Glass-forming ability and corrosion performance of Mn-doped Mg–Zn–Ca amorphous alloys for biomedical applications*. Rare Metals 37(7), 579 (2018); https://doi.org/10.1007/s12598-018-1032-z.

[96] N. Wang, Q. Cao, X. Wang, S. Ding, D. Zhang, J.Z. Jiang, *Ultra-strong and* ductile amorphous-crystalline Ti-Zr-Hf-Nb-Ta/Co-Ni-V nanolaminate thin films. Journal of Alloys and Compounds 973, 172874 (2024); https://doi.org/10.1016/j.jallcom.2023.172874.

[97] S. Wang, T. Xu, Y. Wu, X. Chen, X. Yang, *Brazing Temperature Effects on the Microstructure and Mechanical Properties of Ti-45Al-8Nb Joints Using TiZrCuNi Amorphous Interlayer*. Coatings 14(3), 300 (2024); https://doi.org/10.3390/coatings14030300.

[98] Z.H. Wang, T. Urisu, H. Watanabe, K. Ooi, G.R. Rao, S. Nanbu, M. Maki, M. Aoyagi, *Assignment of surface IR absorption spectra observed in the oxidation reactions: 2H+H_2O/Si (1 0 0) and H_2O+H/Si (1 0 0)*. Surface science 575(3), 330 (2005).

[99] J. Wu, X. Cheng, J. Wu, J. Chen, X. Pei, *The development of magnesium-based biomaterials in bone tissue engineering: A review*. Journal of Biomedical Materials Research Part B: Applied Biomaterials 112(1), e35326, (2024); https://doi.org/10.1002/jbm.b.35326.

[100] H. Yaykasli, B. Avar, M. Panigrahi, M. Gogebakan, H. Eskalen, *Investigation of the Microstructural, Morphological, and Magnetic Properties of Mechanically Alloyed $Co_{60}Fe_{18}Ti_{18}Si_4$ Powders*. Arabian Journal for Science and Engineering 48(1), 845 (2023); https://doi.org/10.1007/s13369-022-07037-4.

[101] H. Yuan, L. Zhou, G.T. Wang, L.B. Zheng, Y.Z. Yang, Si microalloying optimizes the thermal stability, crystallization behaviors and magnetic properties of Fe-rich Fe-B-Cu-Hf alloys. Journal of Magnetism and Magnetic Materials 500, 166339 (2020); https://doi.org/10.1016/j.jmmm.2019.166339.

[102] Y. Zhang, Y. Liu, R. Zheng, Y. Zheng, L. Chen, *Research progress on corrosion behaviors and biocompatibility of rare-earth magnesium alloys in vivo and in vitro*. Journal of Rare Earths 4(12), 1827 (2023); https://doi.org/10.1016/j.jre.2023.03.005.

[103] Q. Zhao, C. Gao, L. Hou, H. Yang, *Emerging Phosphate-Functionalized Co_3O_4/Kaolinite Composites for Enhanced Activation of Peroxymonosulfate*. Inorganic Chemistry 62(12), 4823 (2023); https://doi.org/10.1021/acs.inorgchem.2c04059.

Лусіано Насіменто, Ана Крістіна Фігейредо де Мело Коста

Аморфні сплави, синтезовані методом високоенергетичного подрібнення: дослідження та застосування як біоматеріалів

Лабораторія синтезу керамічних матеріалів, Федеральний університет Кампіна-Гранде, вул. Апрігіо Велозу, 882 — Бодоконго, Кампіна-Гранде 58429-900, Параїба, Бразилія, luciano.uepb@gmail.com

У цій роботі аморфні сплави $Co_{69}Nb_{23}B_8$, $Fe_{78}Si_9B_{13}$, $Co_{68}Cu_{23}B_9$ та $Fe_{64}Nb_{28}B_8$ були синтезовані методом високоенергетичного механоактиваційного подрібнення (ВМП) та досліджені як перспективні біоматеріали для регенерації кісткової тканини. Синтез проводився з навантаженням 20 г при співвідношенні маси куль до порошку 20:1, швидкості обертання 300 об/хв, часу подрібнення 15 год, з використанням етилового спирту (C_2H_6O) як регулювального середника та інертної атмосфери аргону. Аморфні сплави були охарактеризовані методами рентгенівської дифракції (РД), інфрачервоної спектроскопії Фур'є (ІСФ), текстурного аналізу, СЕМ, термогравіметричного аналізу (ТГА), магнітних вимірювань (МВ), механічних випробувань і тестів цитотоксичності in vitro. Ступінь набухання показав позитивні результати, що свідчить про потенціал застосування аморфних Co- та Fe-сплавів у біомедицині. Цитотоксичні дослідження виявили, що безпечна концентрація, за якої життєздатність клітин перевищувала 70%, є перспективною для використання цих матеріалів як металевих біоматеріалів для регенерації кісткової тканини та тимчасових ортопедичних імплантатів.

Ключові слова: аморфні сплави; біомедичні застосування; регенерація кісткової тканини; високоенергетичне механоактиваційне подрібнення (ВМП).